Supporting Information: Electromigrated nanoscale gaps for surface-enhanced Raman spectroscopy

Daniel R. Ward[1], Nathaniel K. Grady[2], Carly S. Levin[3], Naomi J. Halas[3,4], Yanpeng Wu[2], Peter Nordlander[1,4], Douglas Natelson[1,4]

[1]*Department of Physics and Astronomy,*

[2]*Applied Physics Graduate Program,* [3]*Department of Chemistry,*

[4]*Department of Electrical and Computer Engineering,*

and the Rice Quantum Institute, Rice University,

6100 Main St., Houston, TX 77005, USA

(Dated: April 2, 2007)

I. CONTINUUM BACKGROUND

The strong continuum background observed at the nanogaps is shown in Fig. S1A. The continuum slopes down linearly in intensity from 0 cm^{-1} to almost 1500 cm^{-1}. This continuum, seen only in the presence of the nanogap, is compared with the Au film and Si substrate spectra taken using the same microscope configuration. The 300 cm^{-1} and 520 cm^{-1} peaks are from the Si substrate. The spectrum shown in Fig. S1A also shows a small peak at 1345 cm^{-1} which is indicative of absorbates from the air settling at the nanogap. The continuum is localized to the nanogap as seen in Fig. S1B, where a spatial plot has been made by integrating the SERS spectrum from 600 cm^{-1} to 800 cm^{-1} at each point. This wavenumber range was chosen to avoid any of the Si substrate Raman active modes. Additionally a comparison of Fig. S1B with the spatial plot of the Si 520 cm^{-1} peak, Fig. S1C, shows that the continuum background of the nanogap is indeed located at the center of the bowtie, as expected. Although blinking of SERS at the nanogap has been observed for *p*MA and *p*MBA, the continuum itself does not blink in the absence of molecules. This is clear from the data in Fig S1D showing the time evolution of the SERS spectrum at the clean nanogap. No fluctuations are observed, and the continuum background remains constant.

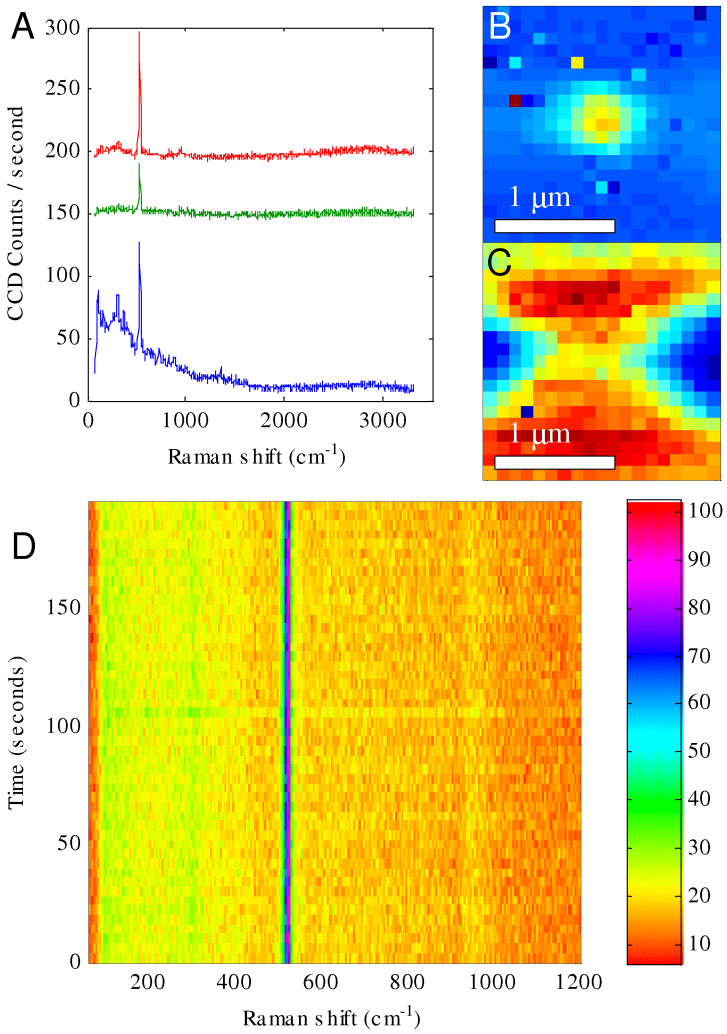

FIG. S1: (A) Raman spectra at hotspot (blue) of a clean bowtie, Au pad(green), and over Si substrate(red). The continuum is very strong at the hotspot and shows linear slope from 0 to $\sim$ 1500 cm^{-1}. Also visible are the 300 cm^{-1} peak and 520 cm^{-1} peaks of the Si substrate and a weak peak at 1345 indicating the onset of atmospheric contamination after approximately 15 minutes of air exposure. Curves have been offset by 150 counts/s (green) and 200 counts/s (red) for clarity. (B) Spatial plot of integrated signal over 600-800 cm^{-1} showing the localization of continuum to the center of the device when compared to the Si plot (C). Yellow is strong signal; blue is no signal. (C) Spatial plot of integrated Si signal over 500-540 cm^{-1}. Red indicates strong Si signal the blue areas show where the Au pads are. (D) Time spectra of clean bowtie. The intensity is reported in CCD counts/second. No blinking of the continuum is observed. The lowest wavenumbers are reported to have zero counts/second due to the low pass filter used to block out the laser.

II. DEPENDENCE ON INCIDENT POLARIZATION

The SERS signal from the nanogap does not have significant polarization dependence, as shown in Fig S2A. The two spectra are from the same nanogap with the polarization at 0 and 90 degrees to the gap. Although slightly different due to positioning and actual time variation of the spectrum, the two spectra do not show any strong differences in the intensities of the *p*MA signal or the continuum. The nanogap *does* exhibit a strong polarization dependence for Rayleigh scattering, as shown in Fig S2B-S2E. Figures S2B and S2D show a spatial map of the Rayleigh scattering for the polarization across the gap (B) and parallel with the gap (D).

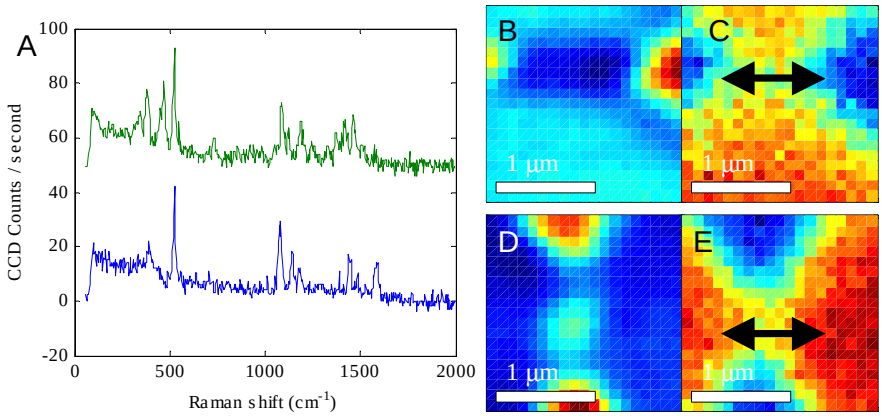

FIG. S2: (A) Raman spectra at hotspot of bowtie with pMA assembled on surface. The blue spectrum is with polarization at 0 deg. (direction shown in (C)). The green spectrum has been shifted 50 counts/s for clarity and is at the same hotspot but with the polarization rotated 90 degrees relative to the substrate (direction shown in (D)). (B) Spatial plot of integrated signal over -40 to 40 cm^{-1} showing the Rayleigh scattering from the center of the device. Red is high intensity blue is low intensity. The large pads are at the left/right. Polarization direction indicated in (C). (C) Spatial plot of integrated Si signal over 500-540 cm^{-1}. Red indicates Si, blue is Au pads. Polarization direction is indicated by the arrow. (D) Spatial plot of integrated signal over -40 to 40 cm^{-1} showing the Rayleigh scattering from the center of the device for the sample rotated 90 deg. relative to (B),(C). Red is high intensity blue is low intensity. Polarization direction is indicated in (E). There is a local maximum in the Rayleigh scattering at the center of the gap. (E) Spatial plot of integrated Si signal over 500-540 cm^{-1}. Red indicates Si, blue is Au pads. Polarization direction is indicated by the arrow.

III. DEPENDENCE ON SOLUTION CONCENTRATION

We have examined SERS spectra for varying supernatant solution concentration during the assembly procedure. Ideally, successive dilutions of the solution should vary surface coverage of the assembled molecules. While molecular coverage on the edges of polycrystalline Au films is not readily assessed, we observe reproducible qualitative trends as concentration is reduced. For *p*MBA molecules assembled from solutions in nanopure water, we have varied concentrations from 1 mM down to 100 pM. The fraction of junctions showing SERS distinct from carbon contamination remains roughly constant down to concentrations as low as 1 μM. For our volumes and electrode areas, this is still expected to correspond to a dense coverage of 1 molecule per 0.19 nm^2. At concentrations below 1 μM, SERS spectra change significantly, while remaining *distinct* from those of carbon contamination: blinking occurs more frequently; modes of b_2 symmetry rather than a_1 symmetry appear more frequently; and the molecular peaks can be more than 100$\times$ larger than the high coverage case for the same integration times. These observations are qualitatively consistent with the molecules exploring different surface orientations at low coverages, and charge transfer/chemical enhancement varying with orientation. However, the actual coverage at the edges remains unknown.

The concentration of the solution used for assembling molecules on the nanogap surface strongly influences the form of the observed Raman spectrum as well as the rate and intensity of the mode blinking. Raman spectra of *p*MBA were taken by soaking samples in 2 mL of different concentrations of *p*MBA. Although for all of these concentrations there are enough molecules in solution to form a monolayer over the bowtie surface, significant differences in the spectra were observed. Fig. S3A shows a representative Raman spectrum for *p*MBA at the nanogap for 1mM concentrations. The two carbon ring modes at 1077 cm^{-1} and 1590 cm^{-1} are clearly present along with a third peak at 1463 cm^{-1}. The time spectra for this nanogap in Fig S3B. The 1077 cm^{-1} and 1590 cm^{-1} peaks are relatively stable and always present while other modes, such as the 1463 cm^{-1} mode, blink on and off for a few seconds at a time. As the concentration is decreased to 1 μM, the *p*MBA signal tends to be stronger with more intense blinking. Additionally the 1077 cm^{-1} mode is observed to disappear while the 1590 cm^{-1} mode remains. Additional modes begin to become more visible such as the 1265 cm^{-1} and 1480 cm^{-1} modes seen in Fig S3C. At even lower concentrations such as 1

nM, the pMBA signal is again more intense with even more blinking as seen in Fig. S3F (which has been plotted with intensity on a log scale). The 1077 cm^{-1} mode is again unseen while the 1590 cm^{-1} mode begins to fluctuate in intensity even more. The blinking becomes much more intense with the intensity of the signal periodically reaching close to ten times the maximum intensity observed for pMBA at 1 μM. We suggest that the increased blinking and larger amplitude signals are a result of the molecules not being as tightly packed on the surface in the 1 μM and 1 nM cases as in the 1 mM case. As a result of looser packing, the molecules are free to explore more surface conformations, including those with more and different charge transfer with the Au surface.

We point out that these pMBA spectra are distinct from those seen in physisorbed carbon contamination on initally clean junctions. These data persist at high incident powers and do not show "arrival" phenomena as described in the subsequent section. Furthermore, they are unlikely to originate from photodecomposition of pMBA, since the illumination conditions are identical for all coverages.

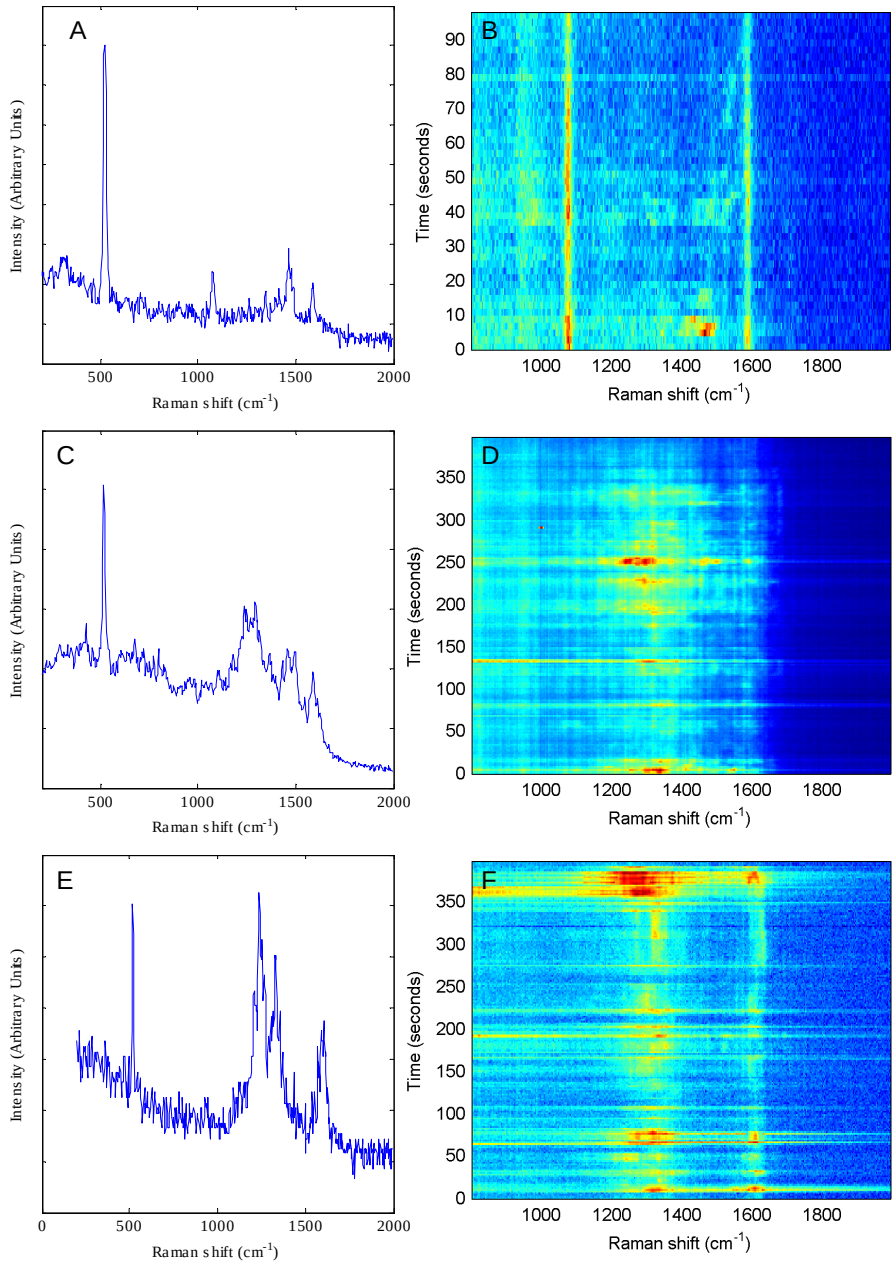

FIG. S3: (A) Raman from pMBA at 1 mM concentration taken at $t = 10$ s. (B) Corresponding time spectrum for 1 mM. (C) Raman from pMBA at 1 μM concentration taken at $t = 251$ s. (D) Corresponding time spectrum for 1 μM. (E) Raman from pMBA at 1 nM concentration taken at $t = 24.5$ s (F) Corresponding time spectrum for 1 nm, plotted on log intensity scale.

IV. DETECTION OF ADSORBED CONTAMINANTS

Due to the large enhancements possible with the nanogaps, contamination from airborne absorbates occurs readily in the absence of assembled molecules on the nanogap surface. We have observed the absorption of contaminants onto the surface of clean nanogaps in as little as 10 minutes. Collecting Raman spectra every 4 seconds, we can observe the appearance of contaminants on the surface as seen in Fig. S4A and S4B. It is difficult to identify the contaminants, as the spectra observed have large variations, although carbon ring modes are often observed in conjunction with other modes. Furthermore the Raman signal from contaminants often blinks *very* strongly, with periods of no or weak signal followed by several seconds of intense blinking, as seen in Fig S4C. The changes in intensity can be more than a factor of 100. Again we suggest that the strong blinking is a result of the weak attachment of the contaminants to the nanogap surface, allowing them to move considerably and explore many interactions with the Au surface. As previously mentioned, these contamination spectra are *not* observed when molecules of interest have been preassembled deliberately on the electrode surface. The likely explanation for this is that the self-assembled later sterically prevents contaminants from arriving at the nanogap region of maximum field enhancement.

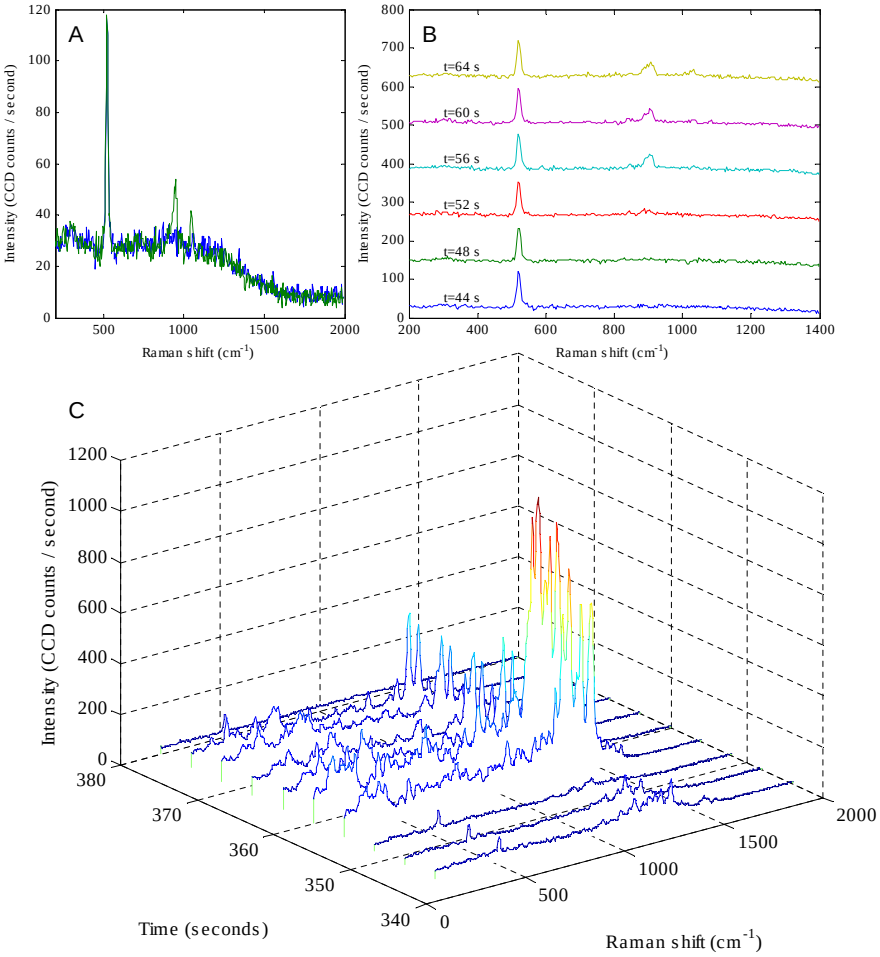

FIG. S4: (A) Raman spectra for clean bowtie (blue) and clean bowtie after a few minutes exposed to the air (green). This change in the Raman spectrum is indicative of contamination for surface absorbed molecules from the air. (B) Raman spectra for a clean bowtie showing the onset of a contaminant signal at 900 cm^{-1} as time progresses. (C) Waterfall plot showing the *extremely* strong blinking observed for adsorbed contamination. The fluctuations are much larger than the those observed for dense coverage of *p*MA, *p*MBA, or P3HT. Notice the scale relative to the 520 cm^{-1} Si peak seen at $t = 340$ s.

V. FDTD CALCULATIONS

The optical properties of the bowtie structure were calculated using the Finite-Difference Time-Domain method (FDTD) using a Drude dielectric function with parameters fitted to the experimental data for gold. This fit provides an accurate description of the optical properties of gold for wavelengths larger than 500 nm.[1] These calculations do not account for reduced carrier mean free path due to surface scattering in the metal film, nor do they include interelectrode tunneling. However, such effects are unlikely to change the results significantly.

The bowtie is modeled as a two finite triangular structures as illustrated in Fig. 4A of the manuscript. Our computational method requires the nanostructures to be modeled to be of finite extent. The plasmon modes of a finite system are standing modes with frequencies determined by the size of the sample and the number of nodes of the surface charge distribution associated with the plasmon. For an extended system such as the bowties manufactured in this study, the plasmon resonances can be characterized as traveling surface waves with a continuous distribution of wavevectors.

A series of calculations of bowties with increasing length reveals that the optical spectrum is characterized by increasingly densely spaced plasmon resonances in the wavelength regime 500-1000 nm and a low energy finite-size induced split-off state involving plasmons localized on the outer surfaces of the bowtie. For a large bowtie, we expect the plasmon resonances in the 500-1000 nm wavelength interval to form a continuous band.[2]

The electric field enhancements across the bowtie junction for the plasmon modes within this band are relatively similar with large and uniform enhancements in the range of 50-150. The magnitudes of the field enhancements were found to increase with increasing size of the bowtie structure. For instance, the maximum field enhancement factor was found to be 115 for a 200 nm bowtie (Each half of the bowtie is modeled as a truncated triangle 200 nm long.) and 175 for a 400 nm bowtie. Our use of a finite gridsize also underestimates the electric field enhancements[3]. Thus our calculated electric field enhancements are likely to *significantly underestimate* the actual electric field enhancements in the experimentally manufactured bowties.

For a perfectly symmetric bowtie, significant field enhancements are only induced for incident light polarized across the junction. If the mirror symmetry is broken, for instance

by making one of the structures thicker or triangular, large field enhancements are induced for all polarizations of incident light.

To investigate the effects of nanoasperities, FDTD calculations were performed for a bowtie with two semi-spherical protrusions in the junction as shown in Fig. 4 of the main text, and Figs. S5-S7 of the Supporting Online Material. As expected, the presence of these protrusions does not influence the optical spectrum. However, the local field enhancements around the protrusions become very large, typically three or four times higher than for the corresponding structure without the defect. The physical mechanism for this increase is an antenna effect caused by the coupling of plasmons localized on the protrusion with the extended plasmons on the remaining bowtie structure[4].

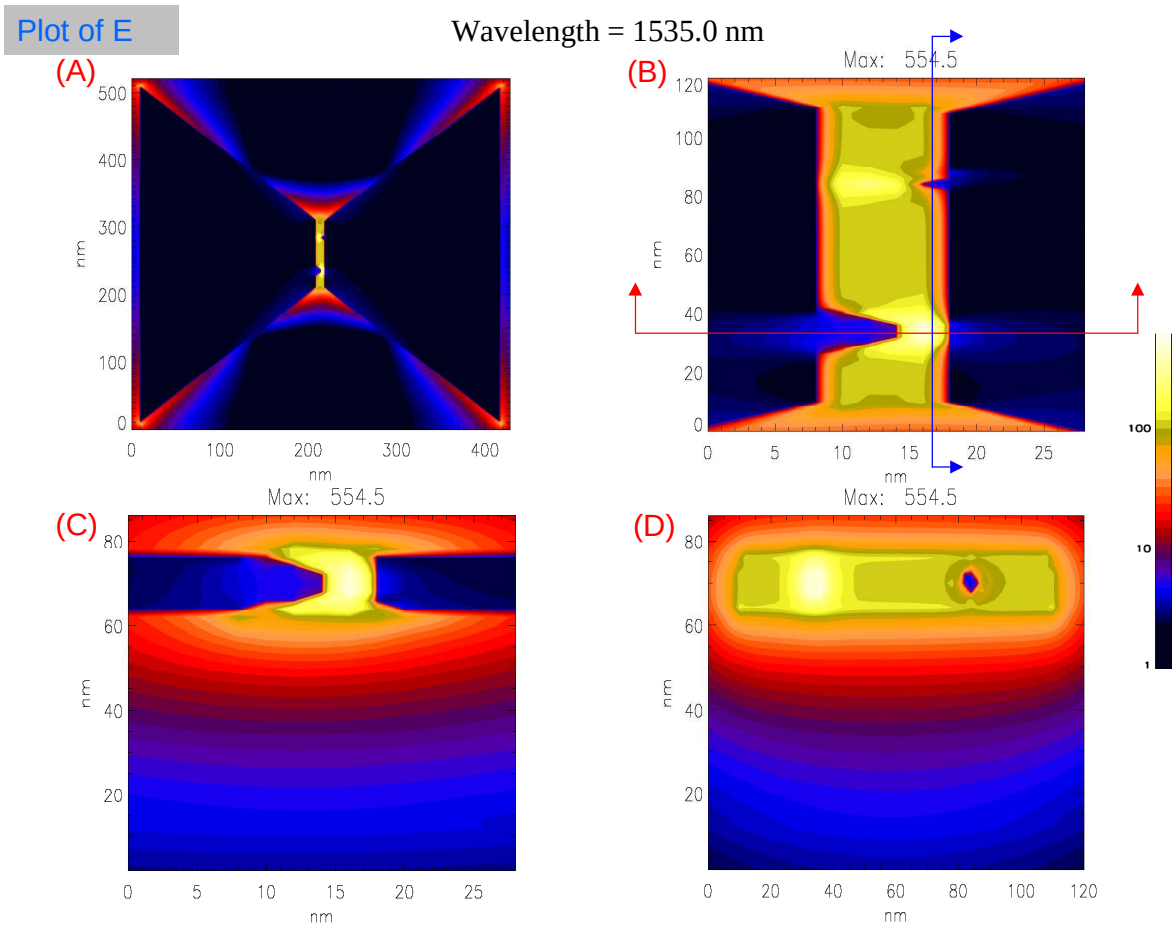

FIG. S5: Maps of FDTD-calculated $|\mathbf{E}|$ for the 1535 nm mode indicated in the main manuscript's Fig. 4A. Color scale is logarithmic in $|\mathbf{E}|/|\mathbf{E}_{inc}|$. Illumination direction is normal incidence, with electric field polarization oriented horizontally in (A)-(C). Maximum *field* enhancements are shown. (A) Overall view. (B) Close-up of interelectrode gap showing asperities. (C) Side-view of section indicated in (B) in red. (D) Side view of section indicated in (B) in blue.

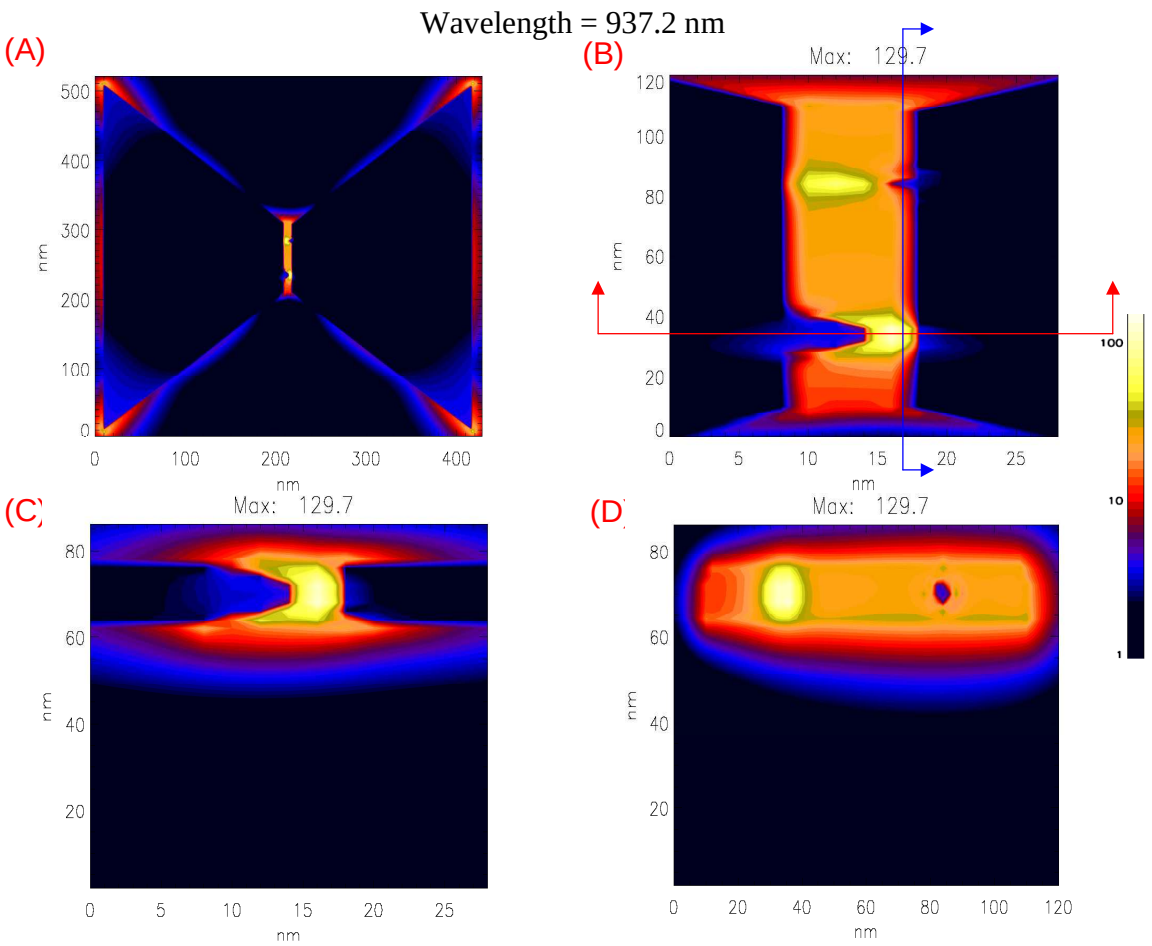

FIG. S6: Maps of FDTD-calculated $|\mathbf{E}|$ for the 937 nm mode indicated in the main manuscript's Fig. 4A. Color scale is logarithmic in $|\mathbf{E}|/|\mathbf{E}_{inc}|$. Illumination direction is normal incidence, with electric field polarization oriented horizontally in (A)-(C). Maximum field enhancements are shown. (A) Overall view. (B) Close-up of interelectrode gap showing asperities. (C) Side-view of section indicated in (B) in red. (D) Side view of section indicated in (B) in blue.

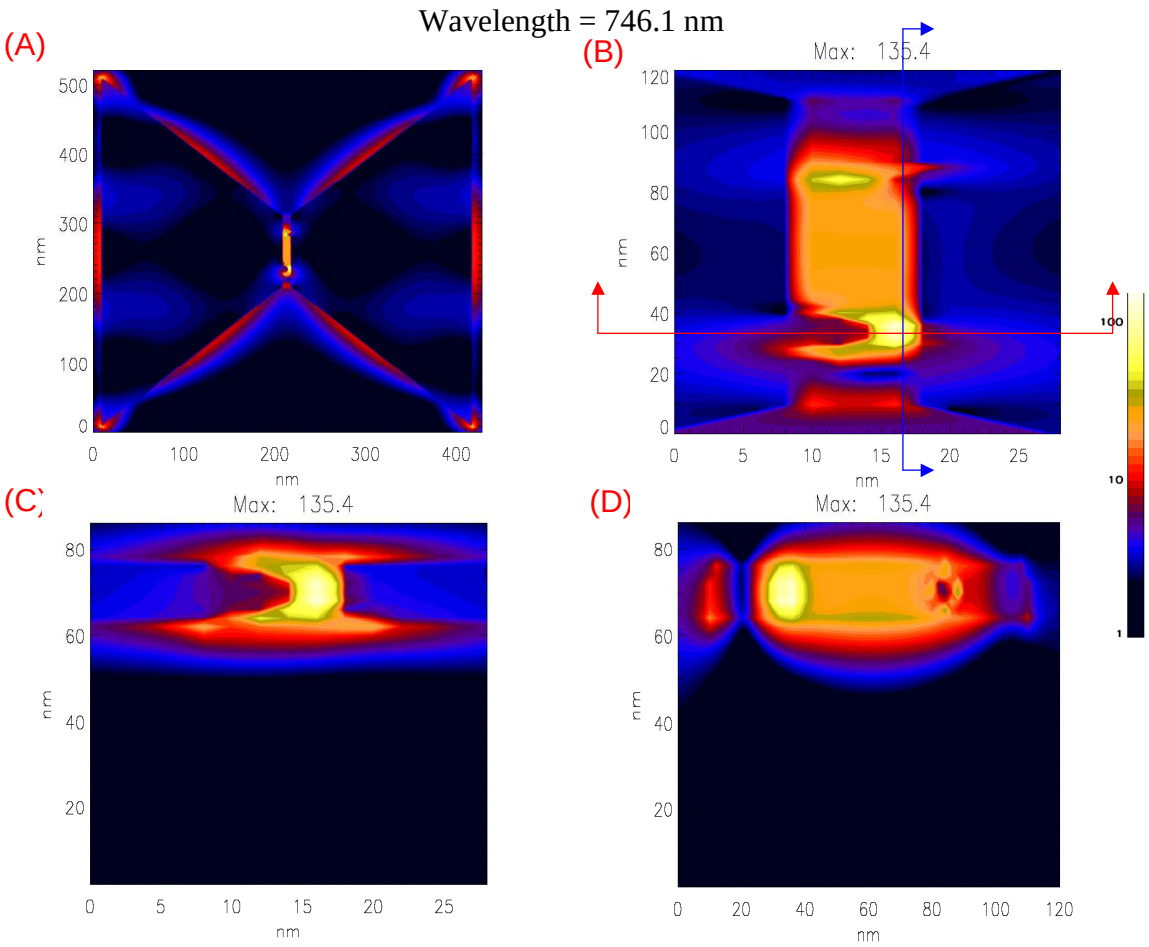

FIG. S7: Maps of FDTD-calculated $|\mathbf{E}|$ for the 746 nm mode indicated in the main manuscript's Fig. 4A. Color scale is logarithmic in $|\mathbf{E}|/|\mathbf{E}_{inc}|$. Illumination direction is normal incidence, with electric field polarization oriented horizontally in (A)-(C). Maximum field enhancements are shown. (A) Overall view. (B) Close-up of interelectrode gap showing asperities. (C) Side-view of section indicated in (B) in red. (D) Side view of section indicated in (B) in blue.

VI. ENHANCEMENT ESTIMATE

To estimate an enhancement based on the data of Fig. 3 in the main text, it was necessary to understand the effective count rate per molecule of Raman scattering from bulk pMA in our measurement setup. This requires knowing the effective volume probed by the WITec system when the laser is focused on a bulk pMA crystal.

The full-width-half-maximum (FWHM) of the laser spot size was found to be 575 nm. This was determined by measuring the count rate of the Rayleigh scattering peak (at zero wavenumbers) as a function of position as the beam was scanned over the edge of a Au film on a Si substrate. Averaging 16 such scans, the Rayleigh intensity was fit to the form of an integrated gaussian to determine the FWHM of the gaussian beam. The 575 nm figure is likely an overestimate due to systematic noise in the flat regions of the fit.

For a gaussian beam with intensity of the form $\propto e^{-\frac{r^2}{2\sigma^2}}$, the FWHM $= 2\sqrt{2\ln 2}\sigma$. The effective radius of an equivalent cylindrical beam is 2σ, or 346 nm in this case. The effective confocal depth[5] was determined by measuring the 520 cm^{-1} Si Raman peak as a function of vertical displacement of a blank substrate. The effective depth profile was determined by numerical integration of the Si data using matlab. The effective volume probed by the beam is 1.92×10^{-12} cm^3. From the bulk properties of pMA, this corresponds to 1.09×10^{10} molecules.

The count rate for the bulk pMA 1077 cm^{-1} line, corrected by the ratio of (Si SERS rate/Si bulk rate) to accomodate for the difference in laser powers, is 46 counts/s, compared with 203 counts/s for the SERS data of Fig. 3. This leads to the enhancement estimate quoted in the main text of 5×10^8.

---

[1] Oubre, C.; Nordlander, P. *J. Phys. Chem. B* **108**, *108*, 17740-17747.

[2] Nordlander, P.; Le, F. *Appl. Phys. B* **2006**, *84*, 35-41.

[3] Oubre, C.; Nordlander, P. *J. Phys. Chem. B* **2005**, *109*, 10042-10051.

[4] Hao, F.; Nehl, C. L.; Hafner, J. H.; Nordlander, P. *Nano Lett.* **2007**, *7*, 10.1021/nl062969c.

[5] Cai, W.B.; Ren, B.; Li, X. Q.; Shi, C. X.; Liu, F. M.; Cai, X. W.; Tian, Z. Q. *Surf. Sci.* **1998**, *406*, 9-22.